Relics of possible (Mg,Fe)3Si2O7 and (Mg,Fe)4Si3O10: potential messengers from the Earth's mantle

Simonpietro Di Pierro, Edwin Gnos, Bertrand Devouard, Pascal Roussel, Damien Jacob, Hugues Leroux

To cite this version:

Simonpietro Di Pierro, Edwin Gnos, Bertrand Devouard, Pascal Roussel, Damien Jacob, et al.. Relics of possible (Mg,Fe)3Si2O7 and (Mg,Fe)4Si3O10: potential messengers from the Earth's mantle. Physics and Chemistry of Minerals, 2026, 53 (1), pp.3. ⟨10.1007/s00269-025-01336-6⟩. ⟨hal-05496163⟩

HAL Id: hal-05496163
https://hal.science/hal-05496163v1

Submitted on 5 Feb 2026

Relics of possible $(Mg,Fe)_3Si_2O_7$ and $(Mg,Fe)_4Si_3O_{10}$: Potential messengers from the Earth's mantle

Simonpietro Di Pierro[1,2], Edwin Gnos[3], Damien Jacob[4], Bertrand Devouard[5], Hugues Leroux[4], Pascal Roussel[6]

[1]Laboratoire de Sciences de la Terre, UMR CNRS 5570, Ecole Normale Supérieure de Lyon, France.
[2]Department of Geosciences, Mineralogy and Petrography, University of Fribourg, Switzerland
[3]Natural History Museum of Geneva, route de Malagnou 1, CP 6434, 1211 Geneve 6, Switzerland.
[4]Univ. Lille, CNRS, INRAE, Centrale Lille, UMR 8207 - UMET, F-59000, Lille, France
[5]Aix-Marseille Université, CNRS, INRA, IRD, Coll France, CEREGE UM34, 13545Aix en Provence, France
[6]Univ. Lille, CNRS, Centrale Lille, Univ. Artois, UMR 8181, UCCS, F-59000, Lille, France

Correspondence to: Simonpietro Di Pierro (simonpietro.dipierro@saint-gobain.com)

Abstract. We discovered a brucite, quartz and moissanite bearing natural rock of mantle affinity containing relics of two now decomposed minerals, so far known from meteorites only, constituting ~4 vol% and scattered in the groundmass of the ~100 gr sample. At the TEM/SAED scale, *phase-I* now consist of porous-less intergrowths of 100-500 nm-sized forsterite-enstatite-Fe-oxide, where $Fo_{99.9}$ and $En_{99.7}$ show both individual and combined [100] and [001] preferred orientations. At the EMPA/WDS scale, *phase-I* shows $(Mg_{2.71}Fe^{2+}_{0.24}Al_{0.02})_{\sum=2.97}(Si_{1.99}Al_{0.01})_{\sum=2}O_7$ composition. We interpret EMPA chemical and TEM structural combined data according to the decomposition reaction $(Mg,Fe)_3Si_2O_7 \rightarrow Mg_2SiO_4 + MgSiO_3 + Fe_xO_y$. At the EMPA/WDS scale *phase-II* corresponds to $(Mg_{3.84}Fe^{2+}_{0.18})_{\sum=4.02}(Si_{2.97}Al_{0.01})_{\sum=2.98}O_{10}$, while at the TEM/SAED scale it consists of 80-90 vol% amorphous material comprising clusters of ~100 nm-sized forsterite. All collected data would suggest former High-Temperature and Ultra-High-Pressure (HT-UHP) phases, now preserved as low-P transformed relics. The mineral precursors would potentially be main constituents of rocky planets' mantle like ours. As their compositions would be very close to the pyrolite (pristine) model mantle, they would be likely common in the deep mantle. Our discovery would open the possibility for fine-tuning models of Earth seismic discontinuities to novel minerals and structures.

Keywords $(Mg,Fe)_3Si_2O_7$ - $(Mg,Fe)_4Si_3O_{10}$ - Moissanite - Silicon carbide - TEM/SAED - EMPA/WDS - Raman spectroscopy - High-Temperature and Ultra-High-Pressure (HT-UHP) - Mantle mineralogy

1 Introduction

Minerals from depths greater than 150-200 km are mainly known from either preserved or decomposed inclusions in diamonds and inferred from those found in pressurized shock veins in meteorites, while they are used by geophysicists to constrain our planet's composition and physical discontinuities. The mantle, 67% by mass and 84% by volume of Earth, is broadly Mg-Fe-(Ca-Al)-Si-O in chemistry, while mineralogically made of only few phases, namely olivine $(Mg,Fe)_2SiO_4$, orthopyroxene $(Mg,Fe)SiO_3$, clinopyroxene $Ca(Mg,Fe)Si_2O_6$, and their denser polymorphs. (Tschauner et al. 2014; Tschauner 2019). These phases show molar $(MgO+FeO)/SiO_2$ (M/Si) ratios of 2 or 1, respectively, and $Mg/(Mg+Fe^{2+})$ ratios (X_{Mg}) of ~0.93. Petrological and geophysical models do not consider significant shifts from this range, while M/Si ratios of 2.5, 1.33 and 1.5, respectively, are observed for elgoresyite $(Mg,Fe)_5Si_2O_9$ (Bindi et al. 2021), for spineloid phases ringwoodite-Q-II $(Mg,Fe,Ca)_4Si_3O_{10}$ (Ma 2023), and for ringwoodite-Q $(Mg,Fe)_3Si_2O_7$ (Ma et al. 2019; Ma et al. 2018; Tschauner and Ma 2023). These three latter structural types have been found in shock veins of the L6 chondrites Suizhou and Tenham and Martian Tissint shergottite, all bridgmanite-bearing meteorites (Tschauner et al. 2014). For ringwoodite-Q and ringwoodite-Q-II, maximum formation conditions of 24-27 GPa and 2700-2800° K and 23-25 GPa and 2200-2400° K have been inferred, respectively. All meteoritic phases have been proposed as potential mantle constituents of Earth and other rocky planets. Noteworthy, they have not been observed experimentally so far.

We report optical, microprobe, Raman and TEM data showing the possible first terrestrial finding of mineral relics showing general formulas $(Mg,Fe)_3Si_2O_7$ and $(Mg,Fe)_4Si_3O_{10}$. They have been discovered in a magnesia-rich (28.49 wt% MgO, 58.2 vol% of brucite by point-counting) natural specimen, also bearing rock-forming quantities of quartz (25.3 vol%) and moissanite SiC (8.4 vol%), also containing calcite, magnesite, phlogopite-*3T*, Cl-brucite, magnesiochromite and Al-rich orthopyroxene (Di Pierro et al. 2003), Supplementary Fig. S1. Noteworthy that comparable moissanite bearing rock fragments has been reported from *(i)* Miocene, picroilmenite, ulvospinel, magnetite, quartz, apatite, anorthite, carbonates, chlorite, and serpentine bearing alkaline basalt tuff (Dobrzhinetskaya et al. 2018), and *(ii)* from quartz-rich fossil beach placers rich in garnet, diopside, and spinel derived from Late Cretaceous alkali-basalt volcanoes at Mt. Carmel, and related Plio-Pleistocene alluvial deposits (Griffin et al. 2021; Griffin et al. 2024), both in Israel and both linked to intraplate volcanism. Our sample was found in Turkey as a loose cobble in an area of alkaline volcanic and lamproitic rocks (see material section), whilst neither the original outcrop nor the petrogenetic link with the local rocks could have been ascertained so far, leaving the question of our sample provenance still open. Very strong evidences of a natural origin, however, have been brought forward in previous studies, namely: 1) our moissanite contains Fe-Ti-Ca-Al-silicides (Di Pierro et al. 2003) not found in synthetic SiC (Ma et al. 2024), and 2) Rare-Earth Elements (REE) bearing Ca-Al-Si-oxides (CAS) showing unequivocal decompression textures (Di Pierro and Gnos 2016); remarkably, included CAS are thermodynamically incompatible to coexist with SiC in an Acheson industrial reactor (Zhou and Telle 2010); 3) moissanite displays $\delta^{13}C$ isotopic values of -20.9 to -31.0‰, matching with ophiolitic and kimberlitic SiC worldwide values (Trumbull et al. 2009; Di Pierro et al. 2003), modelled as discriminating mantle temperatures (Horita and Polyakov 2015) and proposed as subducted organic carbon (Aitchison et al. 2025).

2 Results

Phase-I and *phase-II*, as named hereafter, occur as anhydrous Mg-Fe-Si-O grains 50-100 µm-sized, optically almost isotropic, displaying M/Si=1.5 ($X_{Mg}=0.92\pm0.01$) and 1.33 ($X_{Mg}=0.93\pm0.03$), respectively (Table 1). They have not been observed in reciprocal contact and show three to one modal abundance.

Phase-I forms red-orange, mostly rhomb-shaped or broken, polycrystalline grains, remarkably some show perfect squared sections (Fig. 1 and Fig. 2A-B). At the 1-2µm scale of the EMPA/WDS electron beam *phase-I* shows $(Mg_{2.71}Fe^{2+}_{0.24}Al_{0.02})_{\Sigma=2.97}(Si_{1.99}Al_{0.01})_{\Sigma=2}O_7$ formula, (Table 1 and Table S1), equivalent to a 1:1 mixture of olivine plus orthopyroxene. Indeed, at the 2µm spot size of the laser beam, Raman spectra show main peaks of olivine (825, 857 cm^{-1}), orthopyroxene (1014, 1035 cm^{-1}) and magnetite (213, 326, 480, 686 cm^{-1}) or hematite

(224, 287, 410), Fig. 3. *Phase-I* has been found in textural equilibrium with magnesiochromite (unpublished data) and in contact with, but not included in moissanite (Fig. 1).

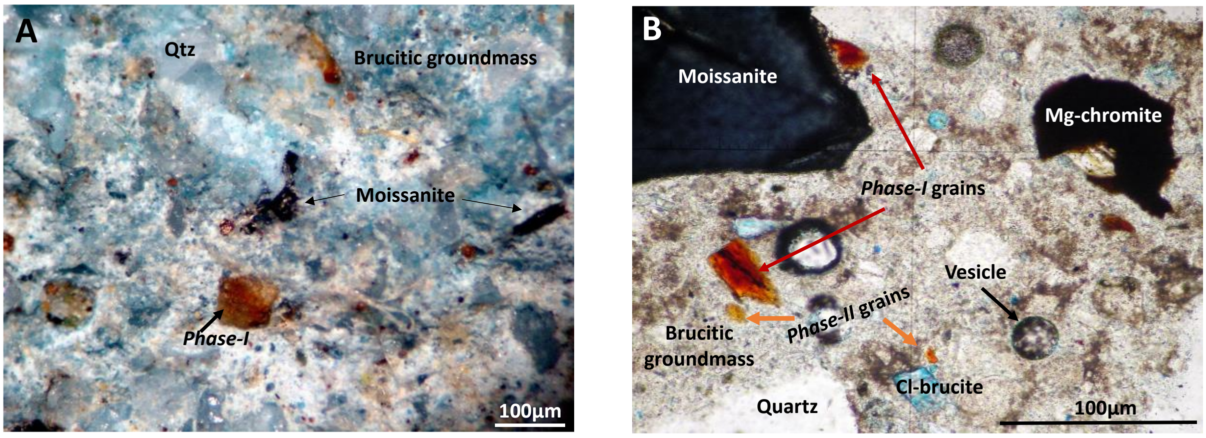

Fig. 1. Optical overview of the Turkish rock specimen. (A) True colors, *phase-I* and *-II* are reddish – orange. Noteworthy the squared shape of the biggest *phase-I*. Black platelets are moissanite (SiC) crystals (8.4 vol%); brucite (58.2 vol%) and grey, vitreous xenomorphic quartz (Qtz; 25.3 vol%) constitute the overall bluish groundmass. (B) Petrographic thin section (transmitted plane-polarized light) overview of the Turkish rock specimen. *Phase-I* grains are reddish, *phase-II* orange pigmented. Dark blue moissanite SiC-*6H* crystal in contact with red *phase-I*, brown Mg-bearing chromite, and quartz (white) are embedded in a fine brucitic matrix (light brown). Light bluish crystals are chlorinated brucite (Di Pierro et al. 2003).

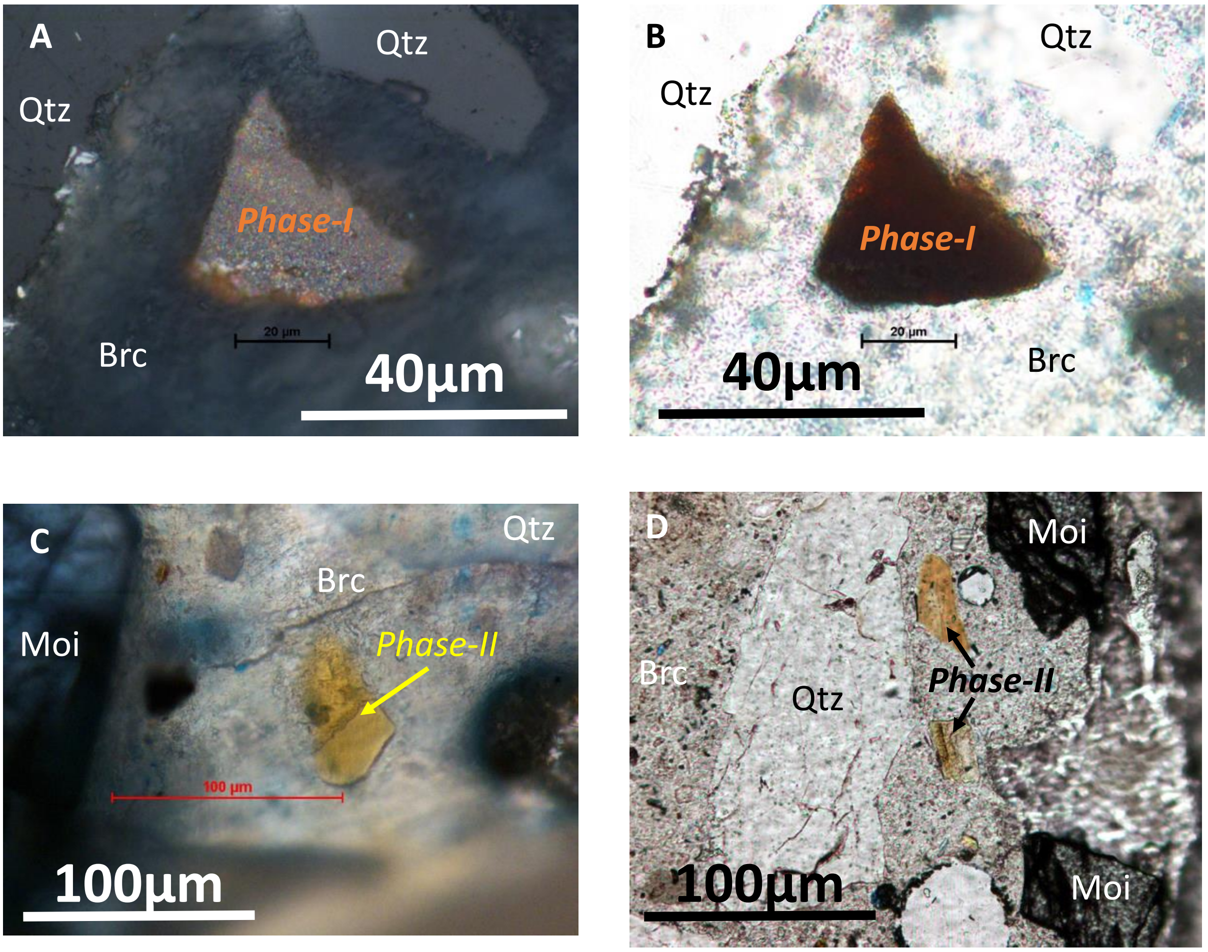

Figure 2. Petrographic thin sections showing *phase-I* and *phase-II*. (A) Reflected light of *phase-I*, $(Mg,Fe)_3Si_2O_7$, showing polycrystalline microstructure, (B) same crystal in transmitted light showing dark red color. (C) and (D) examples of yellow-orange *phase-II* showing ideal $(Mg,Fe)_4Si_3O_{10}$ stoichiometry; (A) and (B) red- and (C) yellow grains have been EMPA/WDS (Table S1), and FIB/TEM analyzed, see Fig. 4-5. Qtz=quartz; Moi=moissanite; Brc=brucite.

Table 1. Selection of representative EMPA/WDS analyses of *phase-I* $(Mg.Fe)_3Si_2O_7$ and *phase-II* $(Mg.Fe)_4Si_3O_{10}$,

	phase-I							*phase-II*						
#	#4/1	#5/1	#8/1	#6/2	#7/2	#8/6	#9/6	#1/6	#3/6	#1/7	#4/7	#17/2	#15/7	#16/7
SiO_2	48.06	48.09	47.45	47.22	48.26	49.24	48.33	51.58	50.93	49.63	49.96	52.74	50.06	49.65
TiO_2	b.d.	b.d.	b.d.	b.d.	b.d.	b.d.	b.d.	b.d.	b.d.	b.d.	b.d.	b.d.	b.d.	b.d.
Al_2O_3	0.72	0.56	0.51	0.47	0.74	0.31	0.31	0.08	0.07	0.08	0.09	1.47	1.94	1.86
Cr_2O_3	0.39	0.28	0.28	b.d.	b.d.	0.06	b.d.	b.d.	b.d.	b.d.	b.d.	0.09	0.10	0.13
FeO*	8.09	8.06	7.79	6.78	7.03	5.41	5.82	3.23	3.68	4.02	3.4	8.19	7.56	7.58
NiO	b.d.	b.d.	b.d.	0.36	0.47	0.38	0.30	0.16	0.29	0.26	0.14	0.26	0.19	0.23
MnO	b.d.	0.12	b.d.	b.d.	b.d.	b.d.	b.d.	b.d.	b.d.	b.d.	b.d.	b.d.	0.13	b.d.
MgO	42.78	43.44	43.65	44.63	43.00	45.02	44.69	44.9	43.44	43.70	43.00	37.86	39.91	39.57
CaO	0.05	0.05	0.04	0.08	0.09	0.10	0.12	0.05	0.08	0.09	0.10	0.10	0.09	0.08
Na_2O	b.d	b.d	b.d	0.05	b.d	b.d	b.d	0.08	0.12	0.18	0.14	b.d	0.07	0.10
K_2O	b.d	b.d	b.d	b.d	b.d	b.d	b.d	b.d	b.d	b.d	0.05	b.d	0.04	0.07
F						b.d	b.d	b.d	b.d	b.d	b.d	b.d	b.d	b.d
Cl						b.d	b.d	b.d	0.09	0.06	0.07	b.d	b.d	0.04
Total	100.09	100.60	99.72	99.59	99.59	100.52	99.57	100.08	98.70	98.02	96.95	100.71	100.09	99.31
	Cations per 7 oxygens							Cations per 10 oxygens						
Si	2.00	1.99	1.98	1.97	2.01	2.01	2.00	2.98	2.99	2.95	2.98	3.07	2.95	2.95
Ti	0.00	0.00	0.00	0.00	0.00	0.00	0.00	0.00	0.00	0.00	0.00	0.00	0.00	0.00
Al	0.04	0.03	0.03	0.02	0.04	0.01	0.02	0.01	0.00	0.01	0.01	0.10	0.13	0.13
Cr	0.01	0.01	0.01	0.00	0.00	0.00	0.00	0.00	0.00	0.00	0.00	0.00	0.00	0.01
Fe^{2+}	0.28	0.28	0.27	0.24	0.24	0.18	0.20	0.16	0.18	0.20	0.17	0.40	0.37	0.38
Ni	0.00	0.00	0.00	0.01	0.02	0.01	0.01	0.01	0.01	0.01	0.01	0.01	0.01	0.01
Mn	0.00	0.00	0.00	0.00	0.00	0.00	0.00	0.00	0.00	0.00	0.00	0.00	0.01	0.00
Mg	2.65	2.68	2.71	2.77	2.66	2.74	2.76	3.86	3.80	3.87	3.83	3.28	3.50	3.50
Ca	0.00	0.00	0.00	0.00	0.00	0.00	0.01	0.00	0.01	0.01	0.01	0.01	0.01	0.01
Na	0.00	0.00	0.00	0.00	0.00	0.00	0.00	0.01	0.01	0.02	0.02	0.00	0.01	0.01
K	0.00	0.00	0.00	0.00	0.00	0.00	0.00	0.00	0.00	0.00	0.00	0.00	0.00	0.01
F	-	-	-	-	-	0.00	0.00	0.00	0.00	0.00	0.00	0.00	0.00	0.00
Cl	-	-	-	-	-	0.00	0.00	0.00	0.01	0.00	0.00	0.00	0.00	0.00
$\sum$	4.98	4.99	5.00	5.01	4.97	4.95	5.00	7.03	7.01	7.07	7.03	6.87	6.99	7.01
X_{Mg}	0.90	0.91	0.91	0.92	0.92	0.94	0.93	0.96	0.95	0.95	0.96	0.89	0.90	0.90
M/Si	1.47	1.49	1.51	1.53	1.44	1.45	1.48	1.35	1.33	1.38	1.34	1.20	1.31	1.32

$(Mg_{2.71}Fe^{2+}_{0.24}Al_{0.02})_{\sum=2.97}(Si_{1.99}Al_{0.01})_{\sum=2}O_7$ (structural formula based on above cations average) or simplified $(Mg,Fe)_3Si_2O_7$.
$(Mg_{3.84}Fe^{2+}_{0.18})_{\sum=4.02}(Si_{2.97}Al_{0.01})_{\sum=2.98}O_{10}$ or simplified $(Mg,Fe)_4Si_3O_{10}$
$(Mg_{3.43}Fe^{2+}_{0.38}Al_{0.12})_{\sum=3.93}Si_{2.99}O_{10}$ or simplified $(Mg,Fe,Al)_4Si_3O_{10}$ if alumina richer
***FeO as Fetot.**
$X_{Mg}=Mg/(Mg+Fe^{2+})$
$M/Si=(Mg+Fe^{2+})/Si$ (mol%)
#: analysis and crystal number
b.d.: below detection

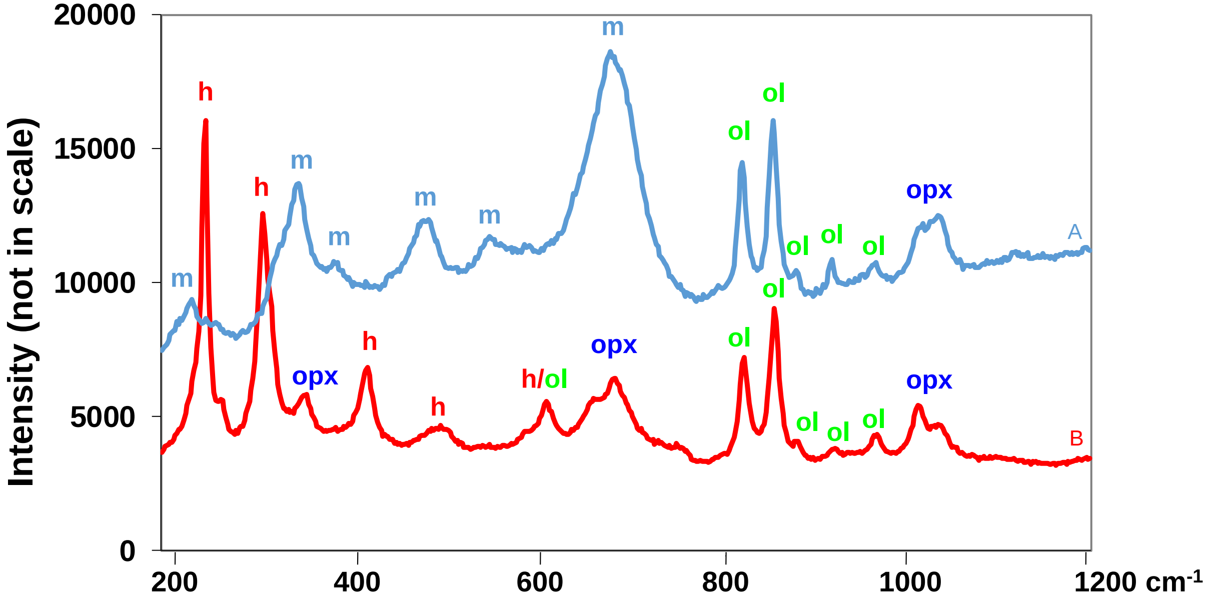

Figure 3. Raman spectra of *phase-I* grains. (A) Mixture of magnetite (m) + olivine (ol) + orthopyroxene (opx); (B) hematite (h) + olivine + orthopyroxene. Peaks position from (Hanesch 2009; Guyot et al. 1986; Huang et al. 2000). *(Gu et al. 2022)*, in their *Suppementary. Database 14 - Inc5b*, report identical Raman spectra of enstatite + olivine (or ringwoodite) ± ferropericlase, intimately associated in seven µm-sized inclusions from Botswana diamond.

At the TEM/SAED scale, *phase-I* consists of an intimate and almost equimolar intergrowths of forsterite ($Fo_{99.9}$) and enstatite ($En_{99.7}$) (Fig. 4A and Table S2). Fe-oxides are confined at grain boundaries (Fig. S2). Remarkably, both forsterite and enstatite are 100-500 nm-sized, their overall microstructure is compact, porous-less, granoblastic polygonal to near-equigranular showing locally 120° triple junctions, characteristic of a metamorphic recrystallization texture. Moreover, the two minerals display both individual and combined [100] and [001] preferred orientations (Fig. 4B-E), indicating parental crystallographic relationship. These nm-scaled forsterite-enstatite-Fe_xO_y intimate and co-oriented intergrowths, at the best of our knowledge are unreported so far, from both natural and synthetic materials literature.

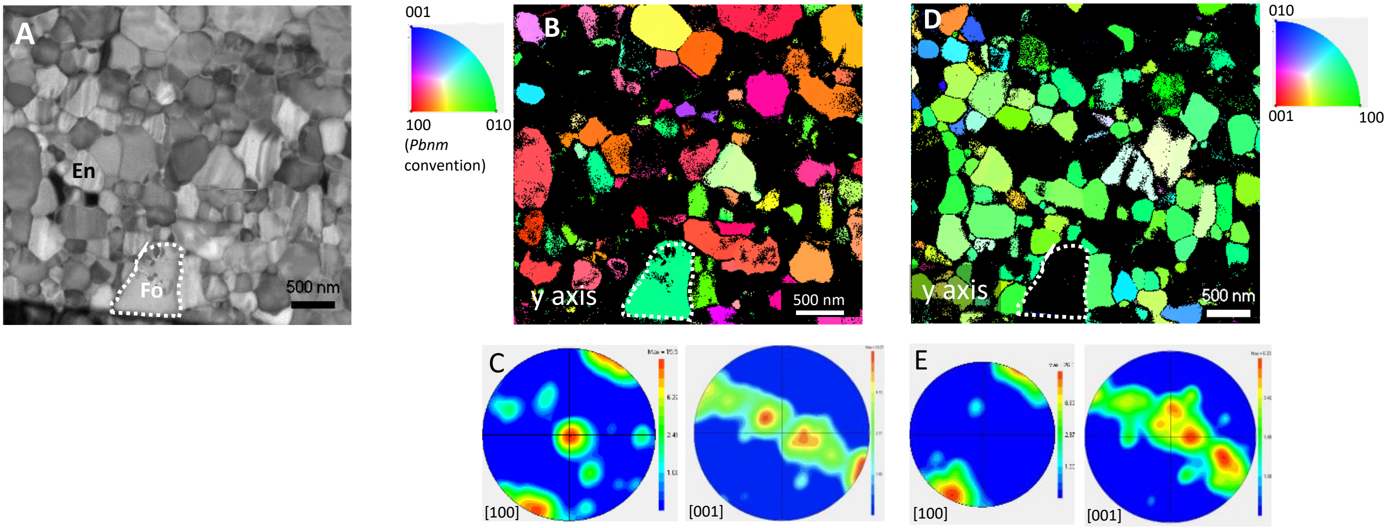

Figure 4. FIB-TEM images of *phase-I*, $(Mg,Fe)_3Si_2O_7$ (same crystal as Fig. 2A-B and Table S1-S2). (A) Correlation index map. All <1µm hypidiomorphic grains of forsterite (Fo), showing uniform grey-shading, and enstatite (En) grains; these latter (orthopyroxene) display some clinoenstatite lamellae responsible for the striated grey contrast. Forsterite are slightly coarser than enstatite crystals, the two phases being evenly dispersed. (B) Forsterite grains' orientation following y-axis (lab. frame). Same area as in (A) (see dotted-white-line-surrounded forsterite grain). (C) Pole figures of forsterite along [100] and [001] showing internally consistent preferred orientation. (D) Enstatite grains' orientation following y-axis (lab. frame), same area as in (A). (E) Pole figures of enstatite along [100] and [001], showing also internally consistent preferred orientation, as well as almost the same preferred orientation as for forsterite grains (Fig. S3).

Phase-II forms yellow-orange lath-shaped grains displaying a characteristic "cleavage", comparable to sheet silicates (Fig. 2C-D), in the direction of the main elongation (Fig. S4). By EMPA/WDS it shows $(Mg_{3.84}Fe^{2+}_{0.18})_{\Sigma=4.02}(Si_{2.97}Al_{0.01})_{\Sigma=2.98}O_{10}$ composition (Table 1), which is the equivalent to a 1:2 mixture of olivine plus orthopyroxene. We also found an Al-bearing variant of *Phase-II* (<2 wt% Al_2O_3, Table 1) showing $(Mg_{3.43}Fe^{2+}_{0.38}Al_{0.12})_{\Sigma=3.93}Si_{2.99}O_{10}$ composition. At the TEM/SAED scale, *phase-II* is 80-90% by volume amorphous, enclosing scattered <1µm aggregates of 100 nm-sized forsterite (Fig. 5). Unlike *phase-I*, no crystals of enstatite have been observed in *phase-II*. Also, *phase-II* displays planar anisotropies parallel to the main elongation, suggesting inherited pattern from the parental mineral. TEM/EDS microanalyses locally show significant shift towards *phase-I* stoichiometry, while measured oxygen excess, 3-4 at%, suggests either minor Fe^{3+} or OH-group in its structure (Fig. S5 and Table S3).

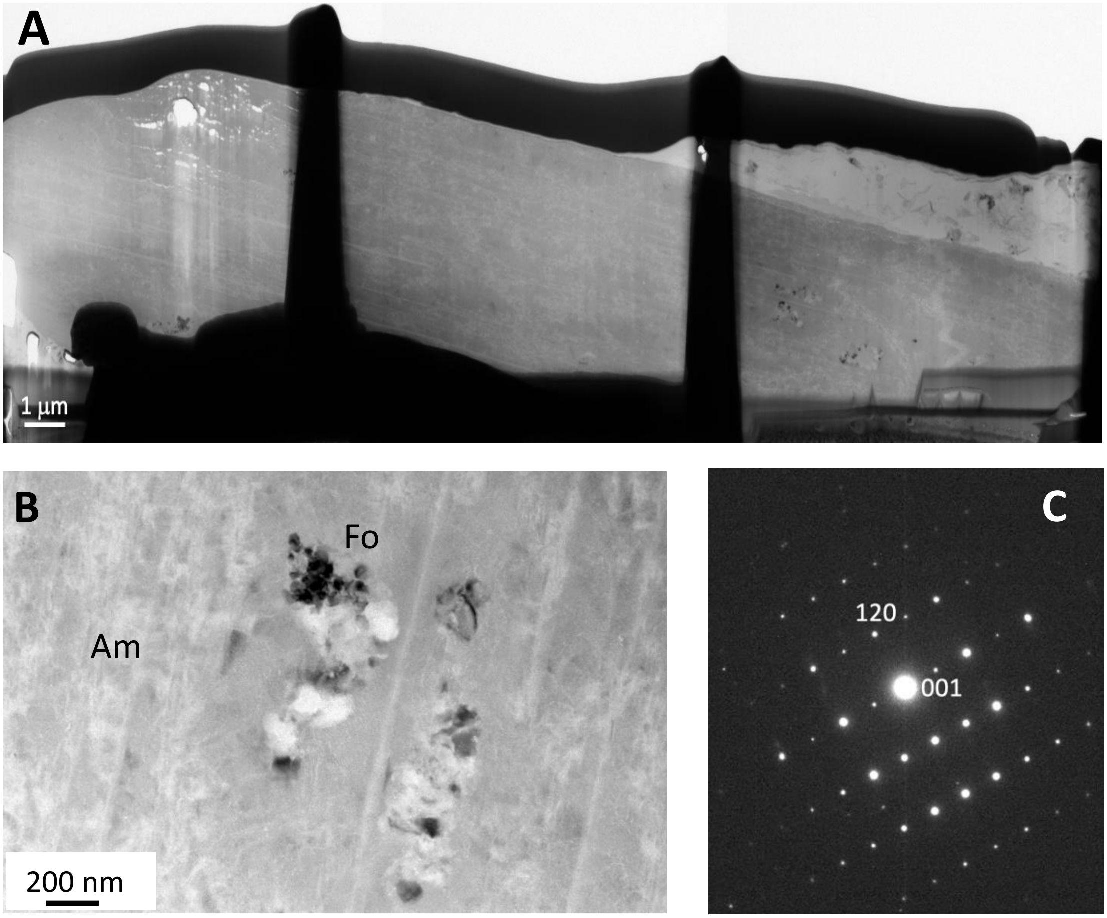

Figure 5. TEM image of *phase-II*, (Mg,Fe)$_4$Si$_3$O$_{10}$, same crystal as Fig. 2C. (A) Lath-shaped crystal showing amorphous (structure-less) matrix. (B) hypidiomorphic grains of forsterite (Fo) within the amorphous (Am) matrix (see also Fig. S3). (C) SAED of a forsterite grain oriented along $[\bar{2}10]$ zone axis.

3 Discussion

The rock specimen that contains *phase-I* and *phase-II* consists of two contrasting mineral assemblages: (i) ~10 vol% of magnesium- and (almost) oxygen-free minerals, namely moissanite containing Fe-Ti-Ca-Al-silicides (Di Pierro et al. 2003) and REE-bearing Ca-Al-Si-oxides (CAS) (Di Pierro and Gnos 2016); and (ii) ~90 vol% of magnesia- and silica-rich, brucite, quartz, here described *phase-I* and *phase-II*, spinels and majorite (unpublished data) showing mantle affinity. This mineral-chemistry contrast is confirmed by the microstructure analysis in thin section since main phases quartz and moissanite are never observed in reciprocal contact (Supplementary Fig. S1), further prompting that the above two assemblages are not at equilibrium. Among the hypotheses raised by Mathez et al. (1995), authors considered moissanite as a relic of reduced primordial Earth, in an otherwise oxidized mantle, for instance.

Within the second mineral assemblage, combined optical, electron microprobe, Raman and TEM investigations show Mg-Fe-Si-O <100 µm-sized grains consisting of [100] and [001] co-oriented intergrowths of 100-500 nm-sized forsterite-enstatite-iron oxides of overall $(Mg,Fe)_3Si_2O_7$ composition, our *phase-I*. Unlike mm- to cm-sized olivine and orthopyroxene showing crystallographic preferred orientation (CPO) in shear stress foliated peridotites (Qi et al. 2018; Tommasi et al. 2006), our rock sample does not show any sign of significant shear deformation (Di Pierro et al. 2003). Moreover, the olivine – orthopyroxene CPO alignment in deformed peridotites is shifted by 15° since the harder enstatite accommodate smaller strain (Tommasi et al. 2006). Mostly amorphous *phase-II*, of $(Mg,Fe)_4Si_3O_{10}$ composition with embedded 100-nm-sized forsterite clusters, is also part of the second mineral assemblage. We interpret both phases as pseudomorphs after denser, unquenched isochemical UHP-HT Mg-Fe-Si-oxides precursors. If correct, our interpretation would imply an overall volume expansion. In agreement with experimental and computational approaches predicting that Fe-bearing silicates (Si in fourfold coordination) are not stable in association with SiC (Mathez et al. 1995; Golubkova et al. 2016; Ulmer et al. 1998; Schmidt et al. 2014; Litasov et al. 2025), in fact, in *phase-I*, $Fo_{99.9}$ and $En_{99.7}$ are both iron-free, since iron-oxides are found confined at grain boundaries (Fig. S2), as if they had been expelled out of the Mg-silicates' structures. Both magnetite and hematite were observed in Raman spectra, in good agreement with the red colour that hematite pigment causes. As all $(Mg,Fe)_3Si_2O_7$ grains are consistently darker red than $(Mg,Fe)_4Si_3O_{10}$, this may indicate that magnetite and hematite could reflect the original Fe^{3+} content.

For *phase-I*, terrigenous or sedimentary origin such as alteration products can be very likely dismissed since incompatible with nm-sized forsterite and enstatite in CPO relationship, and within porous-less 50-100µm larger grains. Likewise, the amorphous state of *phase-II* recalls unquenched set-ups.

UHP minerals from shocked meteorite might be transient and far from equilibrium, but forsterite (ol) + enstatite (opx) + Fe-oxides intimate intergrowths as ours have also been reported as diamonds' inclusions. (Gu et al. 2022) for instance, reported µm-sized polyphase enstatite + olivine (or ringwoodite) ± ferropericlase from seven inclusions in a diamond from Botswana, thought to have generated from transition zone to lower mantle boundary. Analogously, (Nestola et al. 2023) also reported enstatite (former bridgmanite), ferropericlase and Mg-rich olivine (Mg# 99.9) µm-sized inclusion in KK203 super-deep diamond from Kankan, Guinea, that indicates formation in highly variable redox conditions near the 660 km seismic discontinuity. Those above diamonds' inclusions might have also resulted from the breakdown of $(Mg,Fe)_3Si_2O_7$.

4 Possible crystallographic templates for *phase-I* and *phase-II*

Phase-I, $(Mg,Fe)_3Si_2O_7$, and *phase-II*, $(Mg,Fe)_4Si_3O_{10}$, could be pseudomorphs after the spineloid structures ringwoodite-Q (Ma et al., 2018) and ringwoodite-Q-II (Ma et al., 2023) found in shocked meteorites. Recent UHP experiments (Bykova et al. 2016; Lavina et al. 2011; Lavina and Meng 2015; Sinmyo et al. 2016; Ishii et al. 2018) showed that Fe_2O_3, Fe_3O_4 and FeOOH decompose above 10 GPa into a series of mixed-valence Fe-oxides, and many of these phases form solid solution series with Mg-Fe-Si oxides via the coupled substitution 2 Fe^{3+} <-> Mg^{2+} + Si^{4+} (Bindi et al. 2021). Elgoresyite, isostructural to UHP Fe_7O_9 (Sinmyo et al. 2016), would be one such phase in solid solution with $Mg_5Si_2O_9$ (Bindi et al. 2021). The two phases studied here could thus be pseudomorphs after structures denser than spineloids, forming homologous series with the general formula $Mg_{m+n}Si_nO_{m+3n}$ with UHP Fe-oxides (Bindi et al. 2021), as predicted at the terapascal regimes of Super-Earth mantles (Zurkowski et al. 2022). $Mg_3Si_2O_7$ and $Mg_4Si_3O_{10}$ would thus form solid solutions with reported Fe_5O_7 and Fe_7O_{10} (Fig. 6) (Bykova et al. 2016; Lavina et al. 2011; Lavina and Meng 2015; Sinmyo et al. 2016; Ishii et al. 2018). Among these structures the best data exist for the isostructural Fe_7O_9-$Mg_3Fe_4O_9$-$Mg_5Si_2O_9$ solid solution series. Whereas molar volumes for the Mg-Fe-O members vary between 313.25 and 314.46 cm^3mol^{-1}, the molar volume of natural elgoresyite (Bindi et al. 2021) $(Mg_{3.38}Fe^{2+}_{1.60}Ca_{0.02}Si_{1.95}Al_{0.05})O_9$ is 286.94 cm^3mol^{-1}, indicating that this latter should be stable at even higher pressures. Hence, we assume that $Mg_3Si_2O_7$ and $Mg_3Si_4O_{10}$ also would have smaller molar volumes than the corresponding Mg-Fe-oxides. In agreement with data from (Koemets et al. 2021) reporting *P-T* stability of Fe_5O_7 and Fe_7O_{10}, $Mg_3Si_2O_7$ should therefore be stable above minimum conditions of ~40 GPa/1600°K or ~50 GPa/1200 °K, while $Mg_3Si_4O_{10}$ above ~65 GPa and 1800° - 2100° K, i.e. from a depth of 660 km or beneath.

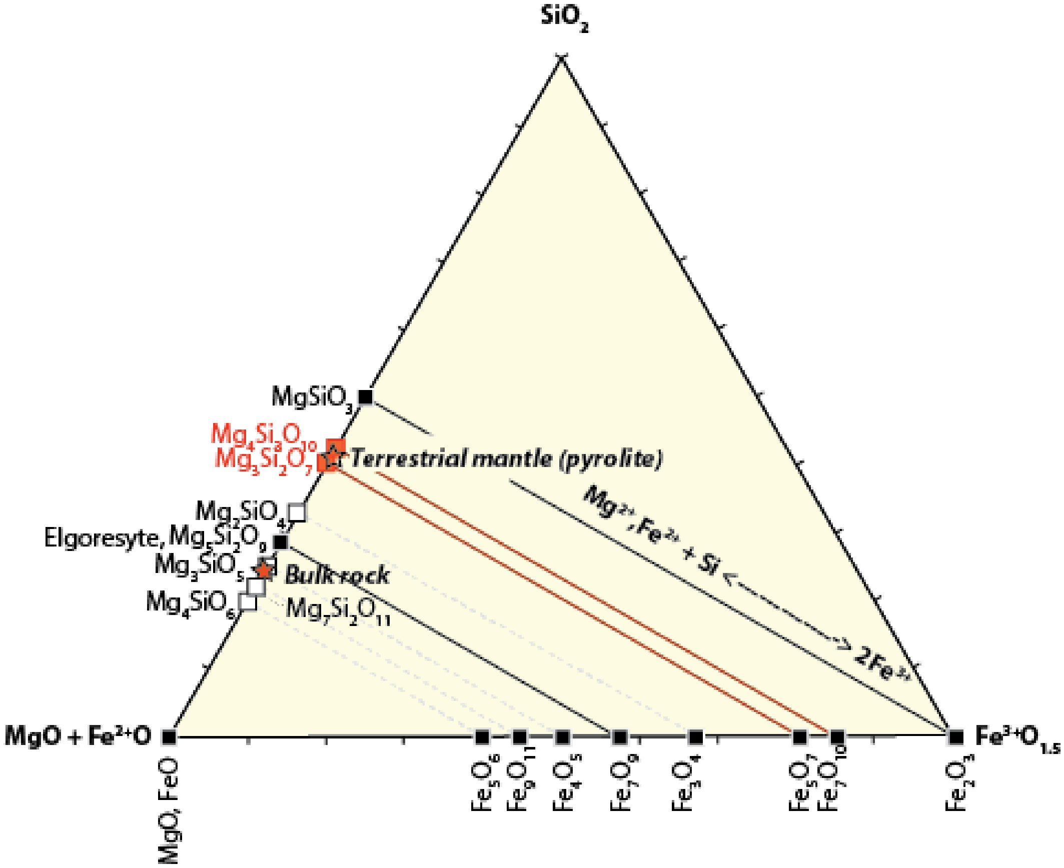

Figure 6. SiO_2-(Mg^{2+}+Fe^{2+})-$Fe^{3+}O_{1.5}$ ternary diagram showing solid solution series of high-pressure Mg-Fe-Si-oxides, modified after (Bindi et al. 2021). Black, solid lines indicated documented isostructural series, the two red lines assumed isostructural series. Filled squares indicate confirmed phases, open squares indicate potentially existing phases. Red squares mark the two Mg-Fe-Si-oxide compositions described in this study and the partially hidden red star the bulk rock composition. Note that both minerals' chemistry plots near the pyrolite mantle model composition (open star), between "enstatite" and "forsterite" compositions. This suggest that they could be important minerals in the terrestrial deep mantle.

Analogously to the $CaTiO_3$-structured perovskite-type $MgSiO_3$ bridgmanite, $(Mg,Fe)_3Si_2O_7$ and $(Mg,Fe)_4Si_3O_{10}$ could also be isostructural with $Ca_3Ti_2O_7$ and $Ca_4Ti_3O_{10}$ layered perovskite structures (Elcombe et al. 1991) and forming a series of $A_{n+1}B_nX_{3n+1}$ general formula (Ruddlesden-Popper type). Whereas in the spineloid structure only part of the Si is six-fold coordinated, all Si is in six-fold coordination in the other two proposed UHP structures.

Looking at the formulas, $(Mg,Fe)_3Si_2O_7$ could be a sorosilicate and $(Mg,Fe)_4Si_3O_{10}$ a silicate that contains an Si_3O_{10} group as in ardennite (Donnay and Allmann 1968). However, no such silicates are known. We suggest that the measured stoichiometry of *phase-I* and *phase-II* grains represent the original composition of this non-quenchable phases. The only phases with such compositions would be potential UHP minerals.

5 Summary and perspectives

For *phase-I*, simplified $(Mg,Fe)_3Si_2O_7$, we obtained TEM/SAED structural data (phase analysis) of its presumably decomposed products, namely nm-sized and showing internal and reciprocal CPO forsterite-enstatite (and Fe-oxide) intergrowths, quantified in roughly 50% each equimolar proportions by cartography, Fig 4 and Fig. S2. Raman spectroscopy (phase analysis) confirmed the coexistence of ol+opx (and Fe-oxide) at the µm-scale of the laser beam. Those analyses well match the chemistry obtained by EMPA/WDS, Table 1 and Table S1, which probes a larger 2-4μm^2 surface. Three independent techniques and their combined data, therefore, would plausibly suggest the following decomposition reaction: $(Mg,Fe)_3Si_2O_7 = (MgFe)_2SiO_4 + (MgFe)SiO_3$, which would explain the previous measures.

Although other interpretations of this data might exist, it would be hard to come up with one that makes more sense and interpret *phase-I* as grains of an unreported mantle mineral that has since decomposed into its lower-P products, as for Botswana (Gu et al. 2022) and Guinea (Nestola et al. 2023) diamonds' µm-sized polyphasic inclusions, peridotitic in character.

Amid the uncertainty concerning our rock specimen provenance, its geological origin is ascertained by its, albeit unusual, mineralogical assemblage of mantle affinity, namely its very high MgO content displayed by brucite in rock-forming quantities, abundant spinels, HP majorite (unpublished data) and 4 vol% of forsterite-enstatite-exsolved Fe-oxides CPO intergrowths, unreported so far, clearly showing crystallographic phase transition character. Even though the original crystal structures are not preserved, the two phases reported here show M/Si ratios very close to the pyrolite model mantle composition (Fig. 6) and can thus expected to be important minerals in the Earth and rocky planets' mantle. If the two phases $(Mg,Fe)_3Si_2O_7$ or $(Mg,Fe,Si)_5O_7$. and $(Mg,Fe)_4Si_3O_{10}$ or $(Mg,Fe,Si)_7O_{10}$ were confirmed by experimental petrology as UHP-

HT mantle minerals as we predict, along with the recently discovered elgoresyite, ringwoodite-Q and ringwoodite-Q-II, they would shed new light on the variety of unknown phases in Earth deep mantle, as predicted for spinel-structured silicates (Koch et al. 2004) and post-perovskite mineralogy (Mosenfelder et al. 2009). All these phases' P-T stability windows need to be constrained by experimental petrology and might be considered in future modelling of the Earth and rocky planets' interiors.

References

Aitchison, J. C., Patias, D., Cluzel, D., Ireland, T. R., Zhou, R., Lian, D., Yang, J., and Yan, Z. (2025) Recycling subducted organic carbon as diamonds: An example from the New Caledonia forearc ophiolite. Geochem. Geophys. Geosyst. 26: e2025GC012250. doi.org/10.1029/2025GC012250

Aldanmaz, E., Gourgaud, A., and Kaymakcı, N. (2005) Constraints on the composition and thermal structure of the upper mantle beneath NW Turkey: evidence from mantle xenoliths and alkali primary melts. J. Geodyn. 39: 277-316. doi.org/10.1016/j.jog.2005.01.002

Aldanmaz, E., Köprübaçi, N., Gürer, F., Kaymakçi, N., and Gourgaud, A. (2006) Geochemical constraints on the Cenozoic, OIB-type alkaline volcanic rocks of NW Turkey: Implications for mantle sources and melting processes. Lithos 86: 50-76. doi.org/10.1016/j.lithos.2005.04.003

Altunkaynak, Ş. and Dilek, Y. (2013) Eocene mafic volcanism in northern Anatolia: its causes and mantle sources in the absence of active subduction. Int. Geol. Rev. 55: 1641-1659. doi.org/10.1080/00206814.2013.792497

Berk Biryol, C., Beck, S. L., Zandt, G., and Özacar, A. A. (2011) Segmented African lithosphere beneath the Anatolian region inferred from teleseismic P-wave tomography. Geophys. J. Int. 184: 1037-1057. doi.org/10.1111/j.1365-246X.2010.04910.x

Bindi, L., Sinmyo, R., Bykova, E., Ovsyannikov, S. V., McCammon, C., Kupenko, I., Ismailova, L., Dubrovinsky, L., and Xie, X. (2021) Discovery of Elgoresyite,$(Mg,Fe)_5Si_2O_9$: Implications for Novel Iron-Magnesium Silicates in Rocky Planetary Interiors. ACS Earth Space Chem. 5: 2124-2130. doi.org/10.1021/acsearthspacechem.1c00157

Bykova, E., Dubrovinsky, L., Dubrovinskaia, N., Bykov, M., McCammon, C., Ovsyannikov, S. V., Liermann, H.-P., Kupenko, I., Chumakov, A. I., and Rüffer, R. (2016) Structural complexity of simple Fe_2O_3 at high pressures and temperatures. Nat. Commun. 7: 1-6. doi.org/10.1038/ncomms10661

Capitani, G. C., Di Pierro, S., and Tempesta, G. (2007) The 6*H*-SiC structure model: Further refinement from SCXRD data from a terrestrial moissanite. Am. Mineral. 92: 407. doi.org/10.2138/am.2007.2346

Di Pierro, S. and Gnos, E. (2016) Ca-Al-silicates inclusions in natural moissanite (SiC). Am. Mineral. 101: 71-81. doi.org/10.2138/am-2016-5357

Di Pierro, S., Gnos, E., Grobety, B. H., Armbruster, T., Bernasconi, S. M., and Ulmer, P. (2003) Rock-forming moissanite (natural α-silicon carbide). Am. Mineral. 88: 1817-1821. doi.org/10.2138/am-2003-11-1223

Dobrzhinetskaya, L., Mukhin, P., Wang, Q., Wirth, R., O'Bannon, E., Zhao, W., Eppelbaum, L., and Sokhonchuk, T. (2018) Moissanite (SiC) with metal-silicide and silicon inclusions from tuff of Israel: Raman spectroscopy and electron microscope studies. Lithos 310-311: 355-368. doi.org/10.1016/j.lithos.2017.04.001

Donnay, G. and Allmann, R. (1968) Si_3O_{10} groups in the crystal structure of ardennite. Acta Crystallogr. B24: 845-855. doi.org/10.1107/S0567740868003274

Elcombe, M. M., Kisi, E. H., Hawkins, K. D., White, T. J., Goodman, P., and Matheson, S. (1991) Structure determinations for $Ca_3Ti_2O_7$, $Ca_4Ti_3O_{10}$, $Ca_{3.6}Sr_{0.4}Ti_3O_{10}$ and refinement of $Sr_3Ti_2O_7$. Acta Crystallogr. B47: 305-314. doi.org/10.1107/S0108768190013416

Golubkova, A., Schmidt, M. W., and Connolly, J. A. D. (2016) Ultra-reducing conditions in average mantle peridotites and in podiform chromitites: a thermodynamic model for moissanite (SiC) formation. Contrib. Mineral. Petrol. 171: 41. doi.org/10.1007/s00410-016-1253-9

Griffin, W., Bindi, L., Cámara, F., Ma, C., Gain, S., Saunders, M., Alard, O., Huang, J., Shaw, J., and Meredith, C. (2024) Interactions of magmas and highly reduced fluids during intraplate volcanism, Mt Carmel, Israel: Implications for mantle redox states and global carbon cycles. Gondwana Research 128: 14-54. doi.org/10.1016/j.gr.2023.10.013

Griffin, W. L., Gain, S. E. M., Saunders, M., Cámara, F., Bindi, L., Spartà, D., Toledo, V., and O'Reilly, S. Y. (2021) Cr2O3 in corundum: ultrahigh contents under reducing conditions. Am. Mineral. 106: 1420-1437. doi.org/10.2138/am-2021-7680

Gu, T., Pamato, M. G., Novella, D., Alvaro, M., Fournelle, J., Brenker, F. E., Wang, W., and Nestola, F. (2022) Hydrous peridotitic fragments of Earth's mantle 660 km discontinuity sampled by a diamond. Nat. Geosci. 15: 1-5.

Guyot, F., Boyer, H., Madon, M., Velde, B., and Poirier, J. P. (1986) Comparison of the Raman microprobe spectra of $(Mg,Fe)_2SiO_4$ and Mg_2GeO_4 with olivine and spinel structures. Phys. Chem. Miner. 13: 91-95. doi.org/10.1007/BF00311898

Hanesch, M. (2009) Raman spectroscopy of iron oxides and (oxy) hydroxides at low laser power and possible applications in environmental magnetic studies. Geophys. J. Int. 177: 941-948. doi.org/10.1111/j.1365-246X.2009.04122.x

Horita, J. and Polyakov, V. B. (2015) Carbon-bearing iron phases and the carbon isotope composition of the deep Earth. Proc. Natl. Acad. Sci. 112: 31-36. doi.org/10.1073/pnas.1401782112

Huang, E., Chen, C. H., Huang, T., Lin, E. H., and Xu, J. A. (2000) Raman spectroscopic characteristics of Mg-Fe-Ca pyroxenes. Am. Mineral. 85: 473-479. doi.org/10.2138/am-2000-0408

Ishii, T., Uenver-Thiele, L., Woodland, A. B., Alig, E., and Boffa Ballaran, T. (2018) Synthesis and crystal structure of Mg-bearing Fe_9O_{11}: New insight in the complexity of Fe-Mg oxides at conditions of the deep upper mantle. Am. Mineral. 103: 1873-1876. doi.org/10.2138/am-2018-6646

Koch, M., Woodland, A., and Angel, R. (2004) Stability of spinelloid phases in the system Mg_2SiO_4–Fe_2SiO_4–Fe_3O_4 at 1100 C and up to 10.5 GPa. Phys. Earth Planet. In. 143: 171-183. doi.org/10.1016/j.pepi.2003.06.001

Koemets, E., Fedotenko, T., Khandarkhaeva, S., Bykov, M., Bykova, E., Thielmann, M., Chariton, S., Aprilis, G., Koemets, I., and Glazyrin, K. (2021) Chemical stability of FeOOH at high pressure and temperature, and oxygen recycling in early Earth history. Eur. J. Inorg. Chem. 2021: 3048-3053. doi.org/10.1002/ejic.202100274

Lavina, B. and Meng, Y. (2015) Unraveling the complexity of iron oxides at high pressure and temperature: Synthesis of Fe_5O_6. Sci. Adv. 1: e1400260. DOI: 10.1126/sciadv.1400260

Lavina, B., Dera, P., Kim, E., Meng, Y., Downs, R. T., Weck, P. F., Sutton, S. R., and Zhao, Y. (2011) Discovery of the recoverable high-pressure iron oxide Fe_4O_5. Proc. Natl. Acad. Sci. 108: 17281-17285. doi.org/10.1073/pnas.1107573108

Litasov, K., Shatskiy, A., Arefiev, A., and Kagi, H. (2025) Reactionary interaction of upper mantle minerals with SiC at 6 GPa and 1100–1500° C: Implication for moissanite appearance in ophiolitic peridotite and other uncommon natural environments. Gondwana Research 141: 102-119. doi.org/10.1016/j.gr.2025.02.005

Ma, C. (2023) Discovery of a new high-pressure silicate, $(Mg,Fe,Ca)_4Si_3O_{10}$ with a spinelloid structure, in a shock melt pocket from the Tissint Martian meteorite. 86th Annual Meeting of the Meteoritical Society 6257.

Ma, C., Tschauner, O., and Beckett, J. (2018) Discovery of a New High-Pressure Silicate Mineral, $(Mg,Fe)_3Si_2O_7$ with a Tetragonal Spinelloid Structure, in Shock Melt Veins from the Tenham Meteorite. Lunar and Planetary Science Conference 49:

Ma, C., Tschauner, O., Bindi, L., Beckett, J. R., and Xie, X. (2019) A vacancy-rich, partially inverted spinelloid silicate,$(Mg,Fe,Si)_2(Si,\square)O_4$, as a major matrix phase in shock melt veins of the Tenham and Suizhou L6 chondrites. Meteorit. Planet. Sci. 54: 1907-1918. doi.org/10.1111/maps.13349

Ma, Y., Miao, M., Chen, M., and Qin, S. (2024) Clarification of Distinguishing Natural Super-Reduced Phase from Synthetics Based on Inclusions. Minerals 14: 722.

Mathez, E. A., Fogel, R. A., Hutcheon, I. D., and Marshintsev, V. K. (1995) Carbon isotopic composition and origin of SiC from kimberlites of Yakutia, Russia. Geochim. Cosmochim. Acta 59: 781-791. doi.org/10.1016/0016-7037(95)00002-H

McNab, F., Ball, P., Hoggard, M., and White, N. (2018) Neogene uplift and magmatism of Anatolia: Insights from drainage analysis and basaltic geochemistry. Geochem. Geophys. Geosyst. 19: 175-213. doi.org/10.1002/2017GC007251

Mosenfelder, J. L., Asimow, P. D., Frost, D. J., Rubie, D. C., and Ahrens, T. J. (2009) The $MgSiO_3$ system at high pressure: Thermodynamic properties of perovskite, postperovskite, and melt from global inversion of shock and static compression data. J. Geophys. Res. Solid Earth 114: B01203. doi.org/10.1029/2008JB005900

Nestola, F., Regier, M. E., Luth, R. W., Pearson, D. G., Stachel, T., McCammon, C., Wenz, M. D., Jacobsen, S. D., Anzolini, C., and Bindi, L. (2023) Extreme redox variations in a superdeep diamond from a subducted slab. Nature 613: 85-89. doi.org/10.1038/s41586-022-05392-8

Nikogosian, I., Gartner, A. B., Van Bergen, M., Mason, P., and Van Hinsbergen, D. J. (2018) Mantle sources of recent Anatolian intraplate magmatism: A regional plume or local tectonic origin? Tectonics 37: 4535-4566. doi.org/10.1029/2018TC005219

Qi, C., Hansen, L. N., Wallis, D., Holtzman, B. K., and Kohlstedt, D. L. (2018) Crystallographic preferred orientation of olivine in sheared partially molten rocks: The source of the “a-c switch”. Geochem. Geophys. Geosyst. 19: 316-336. doi.org/10.1002/2017GC007309

Schmidt, M. W., Gao, C., Golubkova, A., Rohrbach, A., and Connolly, J. A. D. (2014) Natural moissanite (SiC) – a low temperature mineral formed from highly fractionated ultra-reducing COH-fluids. Progress in Earth and Planetary Science 1: 1-14. doi.org/10.1186/s40645-014-0027-0

Sinmyo, R., Bykova, E., Ovsyannikov, S. V., McCammon, C., Kupenko, I., Ismailova, L., and Dubrovinsky, L. (2016) Discovery of Fe_7O_9: a new iron oxide with a complex monoclinic structure. Sci. Rep. 6: 1-7. doi.org/10.1038/srep32852

Tommasi, A., Vauchez, A., Godard, M., and Belley, F. (2006) Deformation and melt transport in a highly depleted peridotite massif from the Canadian Cordillera: Implications to seismic anisotropy above subduction zones. Earth Planet. Sci. Lett. 252: 245-259. doi.org/10.1016/j.epsl.2006.09.042

Trumbull, R. B., Yang, J. S., Robinson, P. T., Di Pierro, S., Vennemann, T., and Wiedenbeck, M. (2009) The carbon isotope composition of natural SiC (moissanite) from the Earth's mantle: New discoveries from ophiolites. Lithos 113: 612-620. doi.org/10.1016/j.lithos.2009.06.033

Tschauner, O. (2019) High-pressure minerals. Am. Mineral. 104: 1701-1731. doi.org/10.2138/am-2019-6594

Tschauner, O. and Ma, C.: Discovering High-Pressure and High-Temperature Minerals, in: Celebrating the International Year of Mineralogy: Progress and Landmark Discoveries of the Last Decades, Springer, 169-206, doi.org/10.2138/am-2024-B1091217, 2023.

Tschauner, O., Ma, C., Beckett, J. R., Prescher, C., Prakapenka, V. B., and Rossman, G. R. (2014) Discovery of bridgmanite, the most abundant mineral in Earth, in a shocked meteorite. Science 346: 1100-1102. DOI: 10.1126/science.1259369

Ulmer, G. C., Grandstaff, D. E., Woermann, E., Göbbles, M., Schönitz, M., and Woodland, A. B. (1998) The redox stability of moissanite (SiC) compared with metal-metal oxide buffers at 1773 K and at pressures up to 90 kbar. Neues Jahrbuch für Mineralogie Abhandlungen 172: 279-307.

Zhou, L. Y. and Telle, R. (2010) Purifying Mechanism in the Acheson Process - A Thermodynamic Study. Mater. Sci. Forum 645-648: 41-44.

Zurkowski, C., Yang, J., Chariton, S., Prakapenka, V., and Fei, Y. (2022) Synthesis and Stability of an Eight-Coordinated Fe_3O_4 High-Pressure Phase: Implications for the Mantle Structure of Super-Earths. J. Geophys. Res. Planets 127: e2022JE007344. doi.org/10.1029/2022JE007344

Material

The specimen has been found as a loose beach pebble of about ~100gr in the neighbourhood of Assos, Biga peninsula, Western Mediterranean cost of Turkey. The sample was collected “by chance” by Salvatore Musacchia who gave it to first author as a curiosity and “because it was pale blue”. Unfortunately, only one unique specimen was found and, despite the lack of evidence, we think plausible that is likely derived, possibly as a xenolith, from Tertiary to Quaternary alkaline volcanic or lamproitic rocks outcropping in the area. These latter are Quaternary (2-0 Ma) intra-continental Ocean Island Basalt (OIB)-type alkaline volcanic eruptions, interpreted as near-primary melt products of adiabatic decompression (Aldanmaz et al. 2005; Aldanmaz et al. 2006) coming from sub-slab asthenospheric mantle. Combined geochemical and petrological (Mcnab et al. 2018; Nikogosian et al. 2018) as well as seismic tomography (Berk Biryol et al. 2011) approaches have inferred that Western Anatolia OIB-type alkali-basaltic volcanism is thought to be triggered by asthenospheric thermal anomalies, driven by regional plate tectonics (Altunkaynak and Dilek 2013). The SiC specimen has been extensively reported (Di Pierro et al. 2003; Di Pierro and Gnos 2016; Trumbull et al. 2009; Capitani et al. 2007).

Methods

In addition to optical microscopy, Electron MicroProbe Analyses (EMPA) equipped with Wavelength-Dispersive Spectrometers (WDS), have been performed at the Institute for Geology, University of Bern, the University Claude Bernard Lyon-1 and Ecole Normale Supérieure (ENS) of Lyon (Joint Laboratory of Earth Sciences), using Cameca SX 50 microprobes. Complementary analyses were obtained at the University of Geneva using a JEOL 8200 microprobe. Operating conditions of all machines were 15 kV and 20 nA, the electron beam was focused to probe 2-4µm^2 of surface and 1-2µm of depth; natural and synthetic silicates and oxide standards were used. Detection limits in element wt% are Si 0.02; Ti 0.03; Cr 0.04; Na 0.03; Al 0.02; Y 0.06; Ce 0.08; La 0.08; Fe 0.07; Ni 0.07; Mn 0.08; Mg 0.03; Ca 0.02; Sr 0.07; Ba 0.08; K 0.02; Na 0.03; S 0.03; and F 0.13 and Cl 0.04. Raman spectra were recorded with a DILOR XY spectrometer equipped with confocal optics and a nitrogen-cooled CCD detector, at the ENS-Lyon. A microscope has been used to focus the excitation laser beam (514 nm lines of a Spectra Physics Ar+ laser) to a 2 µm spot and to collect the Raman signal in the backscattered direction. Collecting times were 20 to 60 s at low power of 2–30 mW, to avoid sample deterioration (not observed during spectra acquisition). Electron-transparent thin foils were prepared with a FIB Dual Beam FEI Strata DB 235 at IEMN-Lille and analysed by Transmission Electron Microscopy on the electron microscopy facility of the Advanced Characterization Platform of the Chevreul Institute. Imaging, diffraction and orientation mapping were achieved on a Thermo-Fischer Tecnai LaB_6 instrument operating at 200 kV equipped with the ASTAR^{TM} tool from NanoMEGAS. For orientation and phase mapping, the TEM was set in the microbeam mode with a spot size of about 10 nm and precession angle of 1°. A Thermo-Fischer TITAN Themis operating at 300kV was used for high angle annular dark field (HAADF) imaging using an electron probe of about 0.1 nm. Quantitative chemical data were obtained using energy dispersive x-ray spectroscopy (EDS) in the scanning transmission electron microscope (STEM) mode and a Super-X windowless, 4 quadrant SDD detector. Hyperspectral elemental maps were recorded, and quantification was performed on selected area of interest. Quantitative data were extracted using the Bruker Esprit software (version 1.9). The Cliff and Lorimer method and an absorption correction were applied assuming a homogeneous thickness of 100 nm. k-factors of the major elements relative to Si were experimentally determined using standard minerals for O, Mg, Al, Ca, Fe.

Acknowledgments: We thank: David Troadec (IEMN) for the preparation of FIB lamellaes, Tom Ruckstuhl and Alexandre Kane for their valuable help in ACOM-TEM data treatment during their 3rd year internship at UMET lab.; Bruno Reynard, Roberto Compagnoni and Bernard Grobéty for encouragement and fruitful discussions. Salvatore Musacchia and Nazarena Oteri are greatly acknowledged for having provided the bluish pebble for research. We thank three anonymous reviewers for their constructive comments and insightfully suggestions, the Editorial Board and editor Taku Tsuchiya for handling the manuscript and their feedback.

Funding: The Chevreul Institute is acknowledged for its help in the development of this work through the ARCHI-CM project supported by the “Ministère de l’Enseignement Supérieur de la Recherche et de l’Innovation”, the region “Hauts-de-France”, the ERDF program of the European Union and the “Métropole Européenne de Lille”. The electron microscopy facility of the Chevreul Institute is also supported by the INSU-CNRS.

Electron-microprobe analyses at the University of Bern were supported by Swiss National Science Foundation (credit 21-26579.89).

Financial support from the Swiss National Science Foundation Commission of the University of Fribourg (fellowship n. PBFR2-101389) to S.D.P. when he was a post-doc fellow at ENS/Lyon is greatly acknowledged.

Author contributions: S.D.P. and E.G. carried out the petrographic and electron microprobe analyses. S.D.P. obtained Raman spectroscopy data. D.J. and H.L. conducted the transmission electron microscopy analyses, including imaging, diffraction and orientation mapping. B.D. and P.R. provided interpretation on TEM analyses. S.D.P. and E.G. wrote the original manuscript. All coauthors improved interpretation and provided editing.

Competing interests: The authors declare that they have no conflict of interest.

Data and materials availability: All data are available in the main text or the Supplementary Information.

Relics of possible $(Mg,Fe)_3Si_2O_7$ and $(Mg,Fe)_4Si_3O_{10}$:

Potential messengers from the Earth's mantle

Simonpietro Di Pierro[1,2], Edwin Gnos[3], Damien Jacob[4], Bertrand Devouard[5], Hugues Leroux[4], Pascal Roussel[6]

[1]Laboratoire de Sciences de la Terre, UMR CNRS 5570, Ecole Normale Supérieure de Lyon, France.
[2]Department of Geosciences, Mineralogy and Petrography, University of Fribourg, Switzerland
[3]Natural History Museum of Geneva, route de Malagnou 1, CP 6434, 1211 Geneve 6, Switzerland.
[4]Univ. Lille, CNRS, INRAE, Centrale Lille, UMR 8207 - UMET, F-59000, Lille, France
[5]Aix-Marseille Université, CNRS, INRA, IRD, Coll France, CEREGE UM34, 13545Aix en Provence, France
[6]Univ. Lille, CNRS, Centrale Lille, Univ. Artois, UMR 8181, UCCS, F-59000, Lille, France

Correspondence to: Simonpietro Di Pierro (simonpietro.dipierro@saint-gobain.com)

Supplemntary information

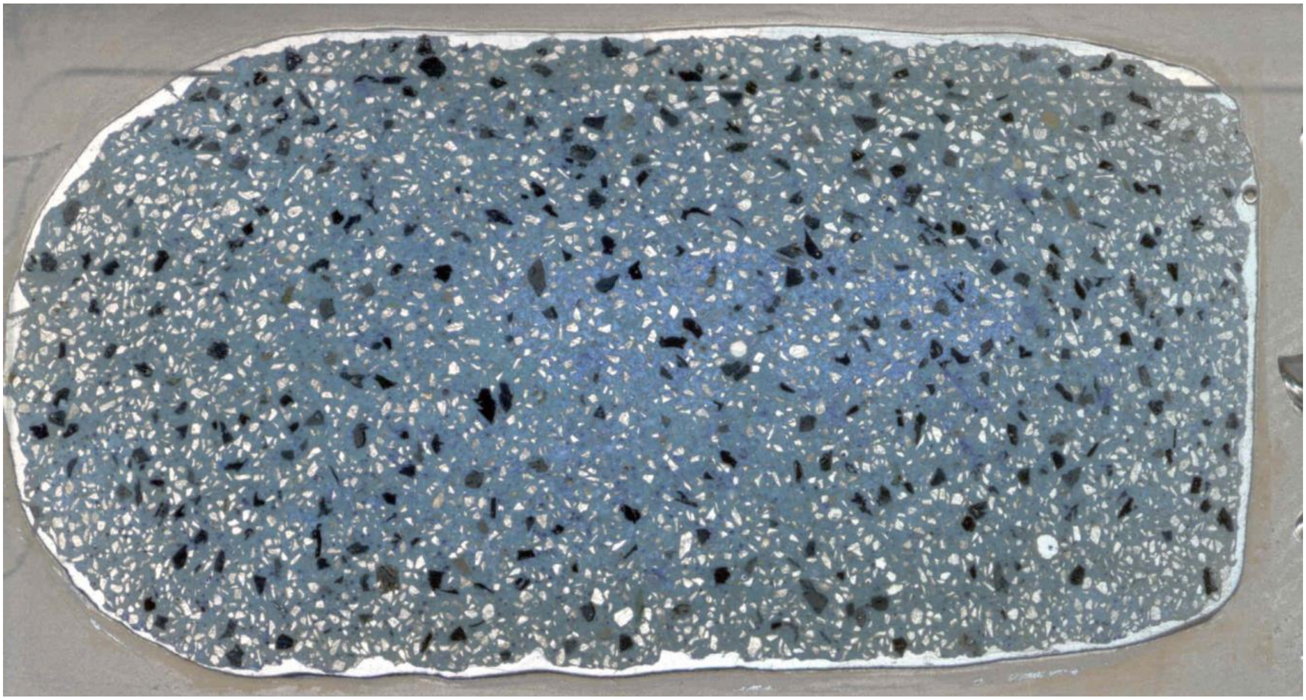

Supplementary Figure S1. Thin section, ~4 x 2 cm^2, of the SiC bearing blue rock from Turkey (same sample of Fig. 1a in (Di Pierro et al. 2003)). Black to dark-grey-colored are moissanite (SiC) crystals, white ones are quartz, pervasive brucitic matrix is bluish. Quartz and moissanite are mm- to sub-mm sized, never observed in reciprocal contact, mostly fragmented even though ipidiomorphic face crystals are abundant. The overall texture is "brecciated", while no overall anisotropies are visible, quartz and moissanite being evenly distributed in the brucite groundmass.

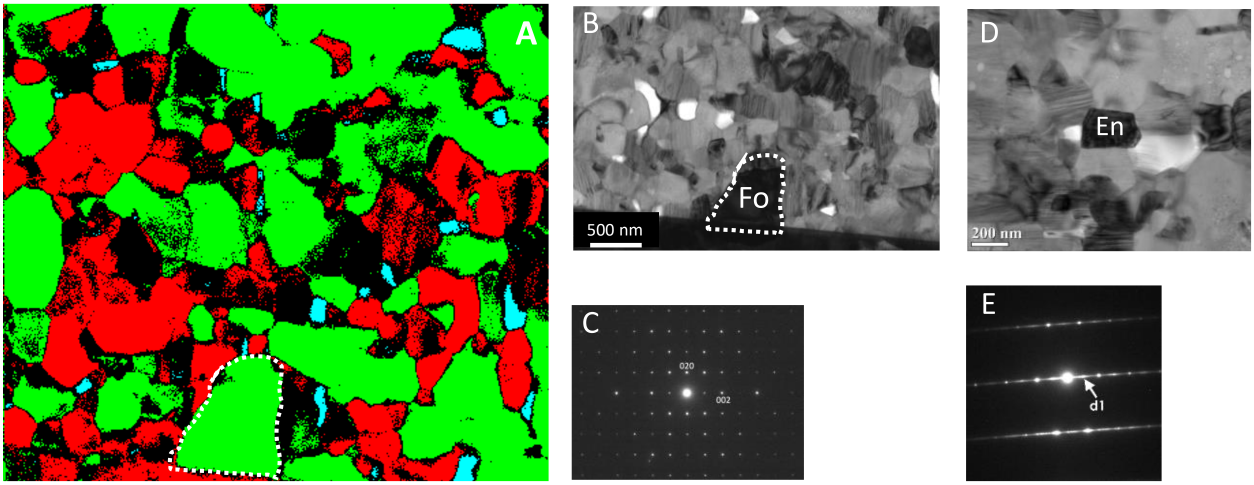

Supplementary Figure S2. FIB-TEM observations of *phase-I*, $(Mg,Fe)_3Si_2O_7$, (A) Phase map of Fig. 4A, trust index >15. Green: Fo, Red: En, Blue: Fe-oxide. Black: unindexed. Fe-oxides are confined at grain boundaries. Neither the oxidation state nor the crystallographic forms of iron-oxides, supposed to be either magnetite or hematite from Raman spectroscopy (Fig. 3 in main text) could be ascertained at the TEM scale thus far. (B) Forsterite (Fo) grain Bragg-zone oriented. Enstatite (En). (C) Selected Area Electron Diffraction (SAED) of forsterite grain in (B) oriented along the [100] zone axis. (D) Enstatite (En) grain Bragg-zone oriented (not in A). (E) Selected Area Electron Diffraction (SAED) of enstatite grain in (D). The smallest distance d1 = 0.9 nm corresponds to either (100) diffracting planes for clinoenstatite or (200) for orthoenstatite. Both phases are possible and orthoenstatite (space group Pbca) has been chosen for phase and orientation mapping (see Fig. 4). Unlike *phase-II*, no planar anisotropies have been observed in *phase-I*.

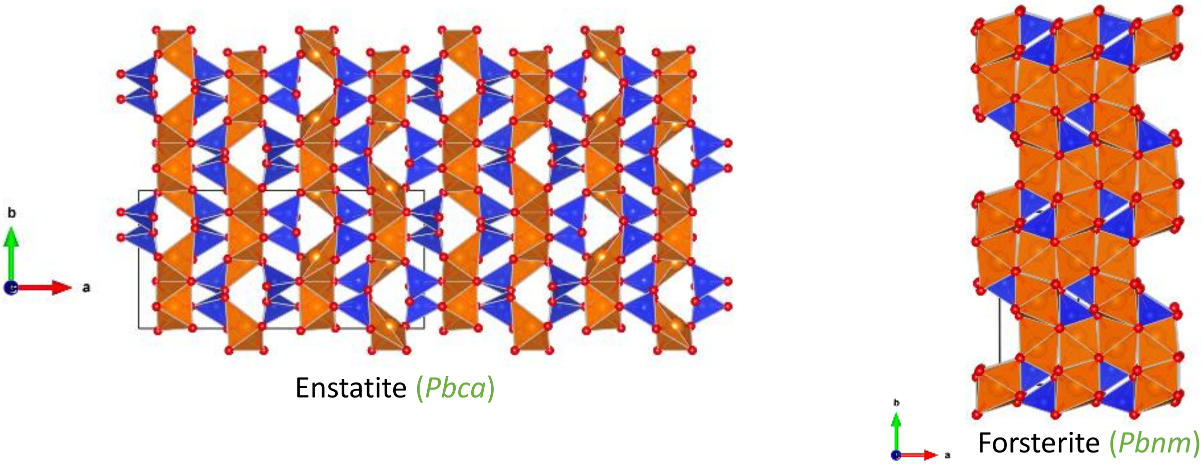

Supplementary Figure S3. Respective crystallographic orientations of enstatite and forsterite (viewed along the c-axes), as suggested from pole figures of Fig. 4C-E.

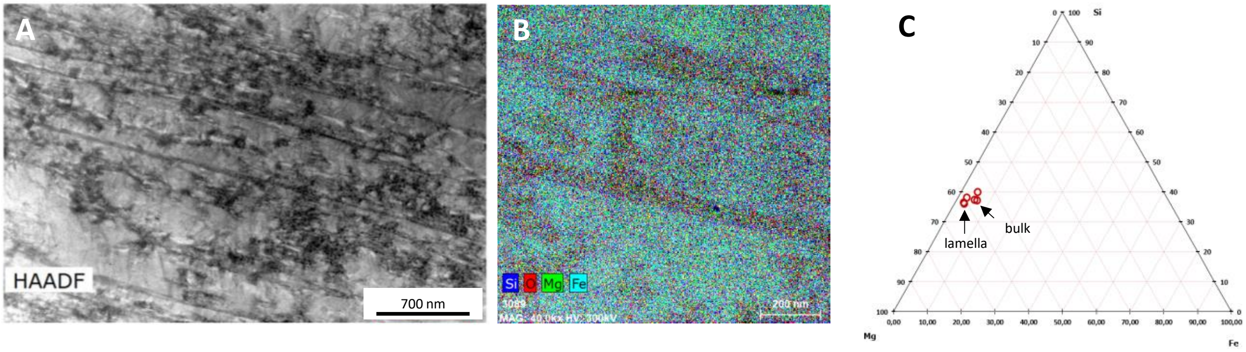

Supplementary Figure S4. FIB-TEM image of *phase-II*, $(Mg,Fe)_4Si_3O_{10}$, same crystal as Fig. 2C. (A) Planar anisotropies (lamellae) parallel to the lath-shaped main elongation, suggesting previous pattern of the parental mineral. (B) EDAX mapping showing Si, O, Mg and Fe distribution. Lamellae are oxygen richer at 3-4 at%, poorer in Al and Fe and higher M/Si.

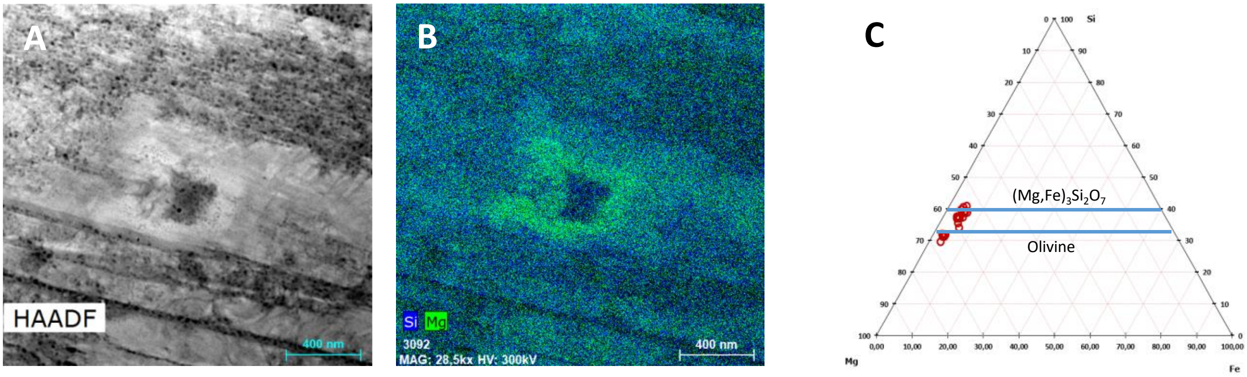

Supplementary Figure S5. FIB-TEM image of *phase-II*, $(Mg,Fe)_4Si_3O_{10}$, same crystal as Fig. 2C. (A) hypidiomorphic grains of forsterite within the amorphous matrix (B) EDAX mapping showing Si, O, Mg and Fe distribution.

Supplementary Table S1

EMPA/WDS analyses of Mg.Fe-silicate *phase-I*.

	phase-I		
	#1	#2	#3
SiO_2	47.87	48.20	49.41
TiO_2	0.02	0.01	0.04
Al_2O_3	0.04	0.02	0.00
Cr_2O_3	0.03	0.00	0.04
FeO*	9.24	8.82	9.33
MnO	0.11	0.11	0.17
MgO	42.49	43.17	41.37
CaO	0.26	0.33	0.58
Na_2O	0.07	0.05	0.09
K_2O	0.04	0.06	0.08
Total	100.17	100.77	101.11
	Cations per 7 oxygens		
Si	2.00	2.00	2.04
Ti	0.00	0.00	0.00
Al	0.00	0.00	0.00
Cr	0.00	0.00	0.00
Fe^{2+}	0.32	0.31	0.32
Mn	0.00	0.00	0.01
Mg	2.65	2.67	2.55
Ca	0.01	0.01	0.03
Na	0.01	0.00	0.01
K	0.00	0.00	0.00
∑	4.99	4.99	4.96
X_{Mg}	0.89	0.90	0.89
M/Si	1.48	1.49	1.41

Same crystals of Fig.2A-B. FIB prepared and SAED analysed, Fig. 4.

$(Mg_{2.63}Fe^{2+}_{0.32}Ca_{0.02})_{\sum=2.97}Si_{2.02}O_7$ (average of above three analyses) or simplified $(Mg,Fe)_3Si_2O_7$

The grain of *phase-II* used for TEM analysis could not be analyzed by EMPA/WDS due to surface charging

#=analysis number

***FeO as Fetot**

XMg=Mg/(Mg+Fe2+)

M/Si=(Mg+Fe2+)/Si (mol%).

Supplementary Table S2
TEM/EDS analyses of forsterite and enstatite.

	forsterite			enstatite		
	a	b	c	a	b	c
Si	13.73	14.50	14.49	20.69	20.99	21.14
Fe	0.04	0.11	0.00	0.19	0.08	0.06
Mg	28.24	26.74	27.40	17.59	17.83	17.86
Ca	1.12	1.40	0.86	1.19	0.60	0.38
O	56.87	57.25	57.25	60.34	60.50	60.57
	100.00	100.00	100.00	100.00	100.00	100.01

Same crystal of Fig.2A-B, FIB prepared, Fig. 4
Forsterite (a) = $(Mg_{2.824}Fe^{2+}_{0.004}Ca_{0.112})_{\sum=2.94}Si_{1.373}O_{5.687}$ simplified $Mg_3Si_{1.5}O_6$ or 2/3 Mg_2SiO_4
Enstatite (c) = $(Mg_{1.786}Fe^{2+}_{0.006}Ca_{0.038})_{\sum=1.83}Si_{2.114}O_{6.057}$ simplified $Mg_2Si_2O_6$ or $MgSiO_3$

Supplementary Table S3
Representative TEM/EDS analyses of *phase II* (amorphous groundmass) and embedded forsterite clusters (at%).

	Amorphous			Forsterite		
	a	b	c	a	b	c
Si	16.00	16.02	15.93	13.39	13.00	13.56
Fe	2.02	2.08	1.89	1.30	1.26	1.20
Mg	22.73	22.62	22.93	27.66	28.19	27.46
Ca	0.07	0.06	0.03	0.02	nd	0.06
Al	0.76	0.75	0.81	0.59	0.70	0.56
Cr	0.14	0.16	0.18	0.13	0.09	0.17
Mn	0.02	0.02	nd	0.02	0.05	0.02
Ni	0.04	0.05	0.03	0.02	0.01	0.01
O	58.22	58.24	58.20	56.87	56.70	56.96
	100.00	100.00	100.00	100.00	100.00	100.01

Same lath-shaped crystal (C) of Fig.2, FIB prepared, Fig. 5
TEM/EDS of *phase-II* and forsterite cluster within
$(Mg_{2.74}Fe_{0.25})Cr_{0.02}Al_{0.10}Si_{1.89}O_7$ or $(Mg_{3.93}Fe_{0.07})(Si_{2.71}Fe_{0.30}Al_{0.14}\ Cr_{0.03})O_{10}$